EES Solar

PAPER

View Article Online
View Journal | View Issue

Cite this: *EES Sol.*, 2026, **2**, 381

Performance measurement of emerging 3- and 4-terminal tandem solar cells

Tao Song, *[a] John F. Geisz,[a] Laurie-Lou Senaud,[b] Lisa Champault,[b] Florent Sahli,[b] Jonas Geissbühler,[b] Bertrand-Paviet Salmon,[b] Quentin Jeangros,[b] Jeremy Brewer,[a] Idris Davis,[a] Rafell Williams,[a] Kaitlyn VanSant[a] and Nikos Kopidakis[a]

Tandem solar cells are not limited to the conventional two-terminal (2-T) configuration. Multi-terminal designs like three-terminal (3-T) and four-terminal (4-T) devices have gained increasing attention in the PV community due to their relaxed current-matching requirement between subcells and their potential for enhanced energy yield. However, reliable and standardized methods for evaluating the performance of multi-terminal tandems remain underdeveloped. This work addresses this gap by providing comprehensive measurement guidelines tailored to these advanced configurations. We examine key coupling mechanisms between subcells, including the shared electrical load in 3-T devices and optical luminescent coupling in both 3-T and 4-T devices, to enable accurate and consistent performance evaluation. Furthermore, we propose two stabilized measurement methods for emerging 3-T tandem cells incorporating perovskite subcells: (1) a two-dimensional maximum-power-point tracking (MPPT) approach that continuously tracks both subcells' maximum power points (P_{MAX}) until convergence to stabilized outputs, and (2) a hybrid approach that combines MPPT for one subcell with stabilized current recording under fixed voltage biases near the P_{MAX} of the other, allowing robust extraction of the overall stabilized P_{MAX} (termed "MPPT + asymptotic P_{MAX} scan" method). These methods directly address the dynamic current responses inherent to perovskite-containing tandems, providing a foundation for meaningful and reproducible performance comparisons.

Received 20th November 2025
Accepted 1st January 2026

DOI: 10.1039/d5el00195a

rsc.li/EESSolar

Broader context

Tandem solar cells are rapidly pushing photovoltaic efficiency limits, with perovskite/Si tandems now surpassing 35% in certified performance. Although most research focuses on monolithic two-terminal designs, multi-terminal (3-T and 4-T) configurations are gaining attention due to relaxed current-matching constraints, higher energy yield, and compatibility with scalable manufacturing. Yet, reliable and standardized performance-measurement practices for these architectures remain underdeveloped, hindering meaningful comparison and slowing technology translation. This work addresses that need by presenting the first comprehensive, experimentally validated measurement framework for emerging multi-terminal tandems. It spans EQE measurement and spectral tuning to ensure junction-by-junction current balance; synchronized and sequential *I–V* methods that correctly handle electrical and optical coupling; and two steady-state strategies capable of reliably characterizing perovskite-containing tandems: a two-dimensional MPPT method and a hybrid MPPT plus asymptotic P_{MAX} scan approach. We demonstrate the equivalence and throughput trade-offs between methods and highlight how to avoid common pitfalls (*e.g.*, inflated 4-T efficiencies when the top cell is left at open circuit). By enabling accurate, reproducible, and comparable measurements across diverse 3-T and 4-T structures, this work strengthens the metrology foundation needed for future IEC/ASTM-style standards and supports the advancement of emerging tandem technologies toward industrial deployment.

1. Introduction

In recent years, the development of tandem solar cells for cost-effective terrestrial applications has grown rapidly, largely driven by the surge of emerging perovskite-based tandems. This progress has led to remarkable efficiency gains with perovskite/Si tandem cells achieving a certified efficiency of 35.0% for a small (1 cm^2) cell and 33.4% for a larger (261 cm^2) wafer-size cell.[1,2] Moreover, tandem solar cells have evolved beyond the conventional 2-terminal configuration, incorporating more diverse designs. Among these, multi-terminal configurations, such as 3-terminal (3-T) and 4-terminal (4-T) devices, are gaining increasing interest in the photovoltaic (PV) community due to their distinct advantages, including relaxed requirements for current matching between subcells and enhanced energy yield.[3] Ease of fabrication is another advantage, especially for 4-T devices where each subcell can be individually fabricated and optimized, with the final 4-T device assembled *via* simple

[a]*The Materials, Chemical, and Computational Science Directorate, National Laboratory of the Rockies (NLR), Golden, Colorado 80401, USA. E-mail: tao.song@nrel.gov*

[b]*Centre suisse d'électronique et de microtechnique (CSEM), Rue Jaquet-Droz 1, CH-2002 Neuchâtel, Switzerland*

mechanical stacking. Earlier examples of these approaches including both epitaxially-grown III–V 3-T tandems and mechanically-stacked III–V on Si tandems in 3-T and 4-T structures have been demonstrated.[4–10] The combination of all-back-contact Si with two contact terminals located at the rear, paired with adaptable emerging PV materials like perovskites for the top subcell, further simplifies the fabrication of 3-T configurations, making the design more accessible to researchers but also to industrialization.[11,12]

However, the performance evaluation of multi-terminal tandem cells introduces additional complexities compared to their monolithic 2-T counterparts. The extra terminals expand the number of variables that must be carefully controlled during electrical performance testing to ensure the results accurately reflect the real-world field conditions. For example, in 4-T cells, a prominent luminescent coupling effect[13,14] from the top subcell may cause an overestimation of the bottom subcell's performance. If the top subcell's terminals are left improperly constrained (*e.g.*, left at open circuit rather than operating at P_{MAX} condition), the performance of the bottom subcell would be overestimated due to the luminescent photocurrent generated from the top cell. Additionally, in 3-T tandem cells, coupling from shared internal resistances can significantly affect device performance measurements if one terminal is left floating or if simultaneous multi-terminal scans are not performed. Geisz *et al.*[15] systematically analysed the relationship between measurement loads and device variables in a prototype all-III–V 3-T tandem cell, highlighting these complexities. The more recent addition of perovskite subcells to 3-T and 4-T architectures[11] introduced the additional complexity of the well-known slow response to an applied voltage,[16,17] which needs to be considered when defining the measurement protocol.

From a testing lab perspective, this paper aims to establish a generalized measurement framework applicable across various types of multi-terminal tandem architectures. We focus on measurement setups that (a) make the process more accessible for researchers and (b) address the additional challenges posed by dynamic current responses in emerging perovskite-based devices. By standardizing performance characterization practices, we seek to enhance measurement accuracy, reproducibility, and comparability, thereby accelerating innovation and deployment of multi-terminal tandem technologies.

2. EQE and spectral irradiance adjustment

Performance measurements of terrestrial PV devices are typically carried out under the standard testing conditions (STC), *i.e.*, AM1.5G solar spectrum with a total irradiance of 1000 W m^{-2} and a cell temperature of 25 °C.[18,19] These conditions establish a consistent basis for meaningful and fair comparison across PV technologies. Because laboratory light sources cannot exactly reproduce the AM1.5G reference spectrum, the test operator must adjust the simulator spectrum so that each junction of the tandem device under test (DUT) generates the same photocurrent as it would under the reference spectrum. Without this adjustment, spectral mismatch between the simulator and reference spectra can introduce significant errors in evaluating short-circuit current (I_{SC}), fill factor (FF) and overall performance, particularly for tandem PV devices in 2-T, 3-T, or 4-T configurations.[14,16,17,20] Our previous work[17,20,21] along with others[22–25] has established a spectral irradiance adjustment framework in which the simulator output is tuned to ensure that each junction of the DUT matches its reference-spectrum photocurrent.

The photocurrent of the DUT is expressed as:

$$I_{DUT} = A\int_0^\infty E(\lambda)SR_{DUT}(\lambda)d\lambda \quad (1)$$

where $E(\lambda)$ is the spectral irradiance (in W^{-1} cm^{-2} nm^{-1}), $SR_{DUT}(\lambda)$ is the spectral responsivity (in A/W) of the DUT, and A is the illuminated area (in m^2 or cm^2). For tandem devices, the photocurrent balance must hold for each junction simultaneously, requiring wavelength-specific irradiance tuning rather than simple total power adjustments. To quantify how well tuning aligns with the reference, the current-matching factor Z_i (called current balance factor in the ASTM standard[25]) for each individual junction represented as "i" is defined as:[20,24]

$$Z_i = \frac{I^{Ref}_{DUT,i}}{I^{Sim}_{DUT,i}} \quad (2)$$

where $I^{Ref}_{DUT,i}$ is the photocurrent of junction i of the DUT under the reference spectrum (*i.e.* AM1.5G) and $I^{Sim}_{DUT,i}$ is the photocurrent of junction i of the DUT under the simulator spectrum with the condition $Z_i = 1 \pm 0.01$ usually required for accurate testing. Because the DUT cannot be measured under the actual reference spectrum during indoor testing, the spectral mismatch factor is introduced:[26]

$$M_i = \frac{\int_0^\infty E_{Sim}(\lambda)SR_{DUT,i}(\lambda)d\lambda \int_0^\infty E_{Ref}(\lambda)SR_{RC,i}(\lambda)d\lambda}{\int_0^\infty E_{Ref}(\lambda)SR_{DUT,i}(\lambda)d\lambda \int_0^\infty E_{Sim}(\lambda)SR_{RC,i}(\lambda)d\lambda} \quad (3)$$

where $SR_{DUT,i}(\lambda)$ is the spectral responsivity of the i-th junction and $SR_{RC,i}(\lambda)$ is the spectral responsivity of a calibrated reference cell used to set the irradiance for the spectral region of the i-th junction of the tandem. The corrected photocurrent of the DUT relative only to measurements under the simulator spectrum using a calibrated reference cell then becomes

$$I^{Ref}_{DUT,i} = \frac{I^{Sim}_{DUT,i}}{M_i}\frac{I^{Ref}_{RC,i}}{I^{Sim}_{RC,i}} \quad (4)$$

To further simplify spectrum optimization, we employ the junction current ratio between junctions i and j:[20]

$$R_{ij} \equiv \frac{Z_i}{Z_j} = \frac{M_j}{M_i} \quad (5)$$

when using a single broadband reference cell,[20,21] the reference-cell currents cancel out so that eqn (5) can be expressed as a function of only M_i and M_j. This ratio can then be rewritten solely in terms of the DUT responsivities and simulator/

reference spectra. Spectral current balance of the tandem DUT under the reference spectrum is achieved when $R_{ij} = 1$ (within tolerance) for all junction pairs.

This spectrum tuning methodology developed for 2-T measurements is also applicable for both 3-T and 4-T tandem devices. However, it is worth noting a key distinction between the two configurations: in 3-T tandems, the two subcells are electrically coupled whereas in 4-T tandems they are electrically independent. Thus, test operators can measure each subcell (junction) sequentially in 4-T tandems, similar to single-junction cells, while controlling the operating condition of the other subcell. If spectrum tuning and/or a multi-source simulator is unavailable, only the simulator's total irradiance can be adjusted to meet STC requirements, not the wavelength-specific spectral shape. This limitation introduces an error that depends on the magnitude of the luminescent coupling (will be discussed later).

As shown in eqn (3)–(5), the spectral responsivity or equivalently the external quantum efficiency (EQE) of each subcell must first be determined to calculate M_i and R_{ij} during the spectral tuning process. Unlike 2-T tandems, the extra terminals in 3-T and 4-T devices enable direct measurement of each subcell's EQE. A critical caveat, however, is ensuring all terminals are properly loaded to avoid measurement artifacts. For example, in a 4-T tandem with strong luminescent coupling in the top subcell, the two leads of the top subcell should be either shorted or held at the P_{MAX} condition with an appropriate load resistor when measuring the EQE of the bottom subcell. This aspect will be further discussed in section 3.2.

In a 3-T device, the EQEs of both subcells can also be measured separately. For instance, in a 3-T series-connected perovskite/interdigitated-back-contact (IBC) Si tandem, the top cell EQE can be measured by contacting the top perovskite lead and the extra lead (called "Z" hereafter to be consistent with previously defined terminology,[27] note this terminal "Z" is different from the current matching factor Z_i of eqn (2)) from the Si subcell sharing the same polarity as the top perovskite lead. The bottom Si cell EQE can be measured directly from its own contact leads. If luminescent coupling is present, the floating lead can be either shorted with the extra Z lead or connected to a resistor load at the P_{MAX} condition as described above.

Additionally, the EQEs of multi-terminal tandems can be characterized in a 2-T configuration. In such cases, proper light and voltage biasing must be applied to ensure that the subcell under test is current-limiting with minimal leakage current, thereby allowing reliable EQE extraction. A detailed methodology for measuring 2-T tandem devices is provided in previous work.[17]

It is also important to emphasize that the DUT temperature must be maintained at STC (25 ± 1 °C) during both EQE measurements and the subsequent electrical performance testing to ensure reliable performance benchmarking, as device parameters are sensitive to temperature variations.[16] Under continuous illumination, stable temperature control can be achieved using a thermoelectric-controlled temperature-stage and/or chilled air circulation, together with a surface-mounted temperature sensor for real-time monitoring. All the measurements should be performed only after the DUT temperature has stabilized at 25 °C.

3. Electrical performance measurement

When measuring current–voltage (I–V) characteristics, the key distinction between 2-T and multi-terminal (3-T or 4-T) tandem devices measurements lies in the number of electrical loads. A 2-T tandem delivers power to a single electrical load, whereas 3-T and 4-T devices supply power to two separate loads that can operate independently. The advantage of this multi-load configuration is that each subcell's power output can be optimized independently, avoiding the current-matching constraint inherent to series-connected 2-T tandems. However, this flexibility introduces additional complexity. Conventional I–V curves with a single load are insufficient to fully capture the performance of 3-T and 4-T tandems, since the subcells' outputs can be coupled. In addition, some PV materials, such as perovskites may change in performance as a function of time.

The electrical performance of PV devices can most simply be measured by biasing the terminals with a variable load (*e.g.*, programmable power supplies, resistor loads) while monitoring current through a precision resistor with a four-wire connection setup. In research laboratories, I–V sweeps are generally performed using a more versatile instrument, a source-measurement unit (SMU) which combines these functions above. Note that these conventional I–V scans have a predetermined, fixed voltage scan rate (typically 50–200 mV s^{-1}), and do not measure the steady-state performance for slow-responding PV devices (will be discussed in section 3.3). In the following discussion, we use SMUs to illustrate how

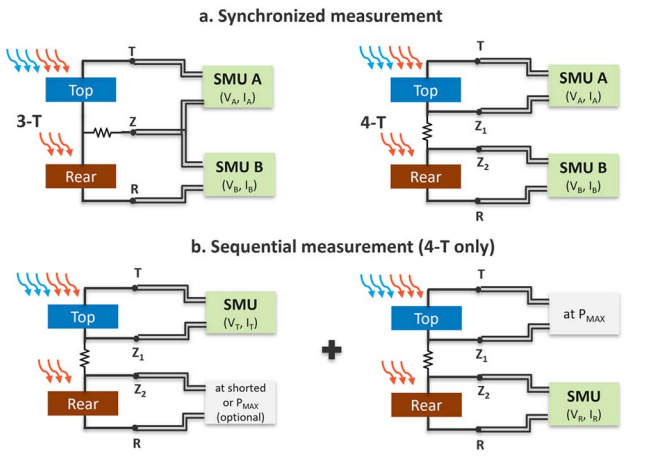

Fig. 1 Schematic of measurement techniques for 3-T and 4-T tandems with a 4-wire connection: (a) synchronized I–V scans with two SMUs A and B, applicable for both 3-T and 4-T configurations. Note that a dual-channel SMU can also be used here to serve as SMU A and SMU B. (b) Sequential I–V scans with a single SMU while untested subcell's two terminals connected with a load resistor representing its P_{MAX}, only applicable to 4-T tandems. Note that device temperature must be controlled at 25 °C (STC) throughout the measurement.

electrical performance measurements are carried out on the multi-terminal tandem cells. Fig. 1 shows the two primary *I–V* measurement approaches for 3-T and 4-T tandems: (a) synchronized scans that require two separate SMUs, and (b) sequential scans using only one SMU. Note that synchronized scans can also be performed with a dual-channel SMU, which integrates two SMUs in one instrument case.[6]

In general, both 3-T and 4-T tandem cells should be characterized using synchronized measurements, meaning all electrical conditions are set and measured simultaneously with two SMUs (A and B). For instance, SMU A and B can be configurated to systematically source voltages V_A and V_B at the corresponding terminals of the cell under test, while simultaneously measuring the resulting currents I_A and I_B. Note that the synchronized voltage and current measurements are essential as the subcells' output are coupled in 3-T and 4-T tandems. The total tandem power at any given time can be expressed as:

$$\begin{aligned} P_{\text{total}}(t) &= P_A(V_A, V_B, t) + P_B(V_A, V_B, t) \\ &= I_A(V_A, V_B, t)\cdot V_A(t) + I_B(V_A, V_B, t)\cdot V_B(t) \end{aligned} \quad (6)$$

In some situations, the nature of the subcell coupling or time-stability can result in simplification of this equation, and thus, the required measurement procedures. For example, the time dependence can be removed if the DUT is time-stable, such as III–V tandems which do not show dynamic current response to voltage bias. In the following sections, we discuss in detail the measurement techniques for 3-T and 4-T tandem cells, as well as the more complex multi-terminal tandems containing perovskite subcells which exhibit dynamic current response. Note that schematics of the multi-terminal devices used in this work are provided in the supplementary material (Fig. S1), and detailed descriptions can be found in ref. 10, 11 and 15.

3.1 3-T devices

Once the illumination spectrum and irradiance are set as described in the previous section, 3-T operation is fully characterized by the three currents and three voltages that are present in the three terminals (*i.e.* T for top, R for rear, and Z for extra), but these are not independent.[15] They are related through Kirchhoff's laws.

$$I_{Ro} + I_{Zo} + I_{To} = 0 \quad (7)$$

$$V_{ZT} + V_{RZ} + V_{TR} = 0 \quad (8)$$

where '*o*' indicates the current flowing out of the cell under test. The operating state of a 3-T tandem can be fully determined by setting any two of these 6 variables (usually voltages), measuring two of the variables (usually currents) and calculating the remaining two from Kirchhoff's laws. Thus, they can be fully characterized with just two SMUs A and B as shown in Fig. 1a. The two loads can equivalently be connected to the 3-T device using any of the terminals in common as described in Geisz's work,[15] but the common-Z (CZ) mode as a function of the subcell voltages is often the most intuitive approach, and will be used in this paper.

Both electrical and optical coupling may be important for 3-T tandems. Optical coupling, also known as luminescent coupling (LC), occurs when light is emitted from the top subcell and reabsorbed in the bottom subcell as photocurrent, thus changing I_B in eqn (6). Typically, optical coupling only transfers current from the top to bottom subcells, since light emitted from the bottom subcell is usually at a lower energy than the top subcell's bandgap, therefore the top subcell is transparent to this low-energy light. Electrical coupling occurs when current flow through a common resistance causing a voltage drop on both subcells as pictured in Fig. 1a left. Electrical coupling causes the operating point of each subcell to influence the performance of the other. In the case of time-stable PV materials such as III–Vs or silicon, eqn (6) simplifies to

$$P_{\text{total}}(t) = I_A(V_A, V_B)\cdot V_A + I_B(V_A, V_B)\cdot V_B \quad (9)$$

as it becomes invariant with time.

Fig. 2 shows the 2-D power contour plot of a series-connected GaInP/GaAs 3-T cell with a device size of around 5 mm × 5 mm, featuring an "n-on-p" polarity in both subcells,[15] plotted as a function of two load voltages (*i.e.*, $P - V_{A,TZ} - V_{B,RZ}$) measured under the common-Z (CZ) mode. This contour is constructed from data points obtained through two synchronized conventional *I–V* scans, with both voltage variables sourced simultaneously. Negative power values are excluded from the plot, since they correspond to power consumption rather than generation—an operating regime irrelevant for solar cells. As expressed in eqn (9), each power point in the contour depends on the two sourcing voltages from the SMUs; thus, precise synchronization of voltage sourcing and current measurement is essential to accurately capture the full electrical and optical coupling mechanisms of the DUT.

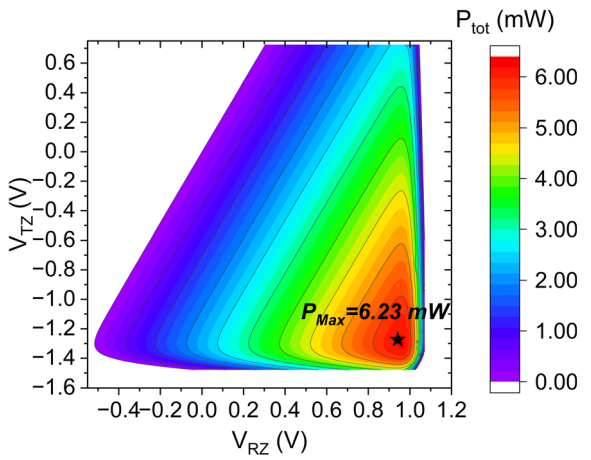

Fig. 2 2-Dimensional (2-D) power plot of a series-connected GaInP/GaAs 3-T tandem solar cell measured under AM1.5G illumination as a function of V_{TZ} and V_{RZ} in common Z (CZ) mode with synchronized conventional *I–V* scans.

In practice, synchronized *I–V* scans must occur concurrently to obtain the corresponding V_A, I_A, V_B, and I_B. Several approaches can be employed to conduct such synchronization. One option is to program the two SMUs to simultaneously source two voltages V_A and V_B at the corresponding terminals (V_{TZ} and V_{RZ} in Fig. 2), measure the resulting voltages and currents, and traverse the entire voltage matrix with a predefined step size to generate the full power mapping. Alternatively, one can hold V_B constant while sweeping V_A across its full range, recording measured I_A, V_A, I_B, and V_B simultaneous at each step *via* hardware triggering, and then repeat this process for successive values of V_B. This work adopts the latter approach, which produces the power mapping shown in Fig. 2.

3.2 4-T devices

4-T tandem cells have two terminals on each subcell, as shown in Fig. 1b, greatly simplifying the *I–V* measurement with sequential scans for each subcell. However, simply summing the efficiencies of the two subcells taken at different times does not accurately represent the tandem cell's actual performance, additional load resistors are required for precise measurement (will be detailed later).

Although the electrical coupling is negligible in 4-T tandems due to the high resistance that separates the two subcells, optical coupling through luminescence can still occur, boosting the photocurrent of the bottom subcell under test depending on the operating conditions of the top subcell. For instance, the EQE of the bottom Si subcell of a GaAs/Si 4-T cell[10] (Fig. 3a) shows a prominent QE tail at short wavelengths (red dashed line) when the top GaAs subcell operates under open circuit conditions. Likewise, Fig. 3b highlights this effect in the *I–V* measurements, where the short-circuit current (I_{SC}) of the bottom Si cell is artificially boosted from 11.5 mA to 15.8 mA due to the luminescence from the top cell at open-circuit condition. As mentioned previously, when the subcell bandgaps decrease through the tandem, optical coupling is not bidirectional, so for highly stable PV materials eqn (6) reduces to

$$P_{total}(t) = I_A(V_A)\cdot V_A + I_B(V_A, V_B)\cdot V_B \quad (10)$$

where the performance of the top subcell is not affected by the conditions of the bottom subcell but the current of the bottom cell can be affected by the top cell's operating conditions.

Consequently, the performance of the top subcell can be characterized with a single SMU first, irrespective of the conditions of the bottom subcells. However, the performance of the bottom subcell should be characterized with a single SMU while the conditions of the top subcell are constrained to the maximum power point of the top subcell previously measured using a simple load resistor as shown in Fig. 1b. The sum of these two maximum powers is the performance of the tandem when both subcells operate at their respective V_{MAX} conditions.

As shown in Fig. 3b, when measuring the independent performance of each subcell in a 4-T tandem, it is crucial to first measure the top subcell to determine the top subcell P_{MAX} conditions to use while measuring the bottom subcell. Otherwise, it could lead to inflated total cell efficiency values (dashed curves in Fig. 3b).

Alternatively, the performance of a 4-T tandem can be measured using two synchronized SMU loads, similar to the approach for 3-T cells in section 3.1. This will give the same maximum power results as the simplified sequential *I–V* scan

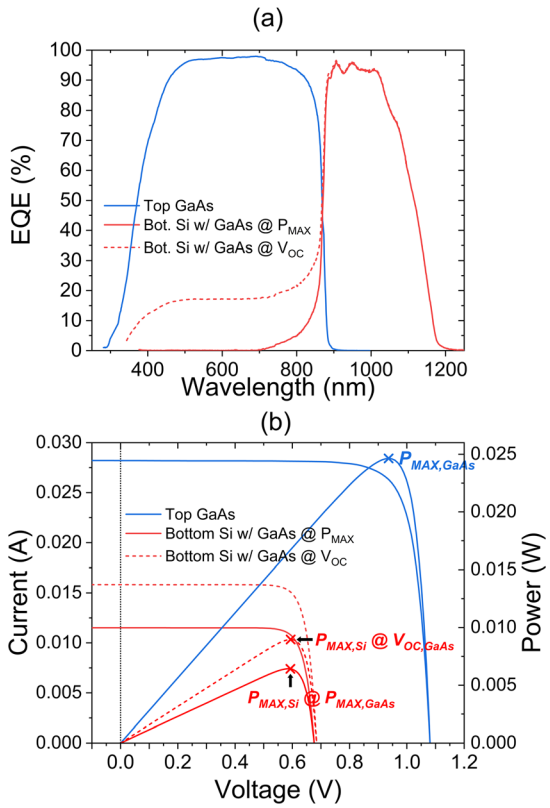

Fig. 3 Effects of luminescent coupling (LC). (a) EQEs and (b) light *I–V* and *P–V* curves of a GaAs/Si 4-T tandem cell. The bottom Si subcell were measured while the top GaAs was held under both P_{MAX} and open-circuit (V_{OC}) conditions.

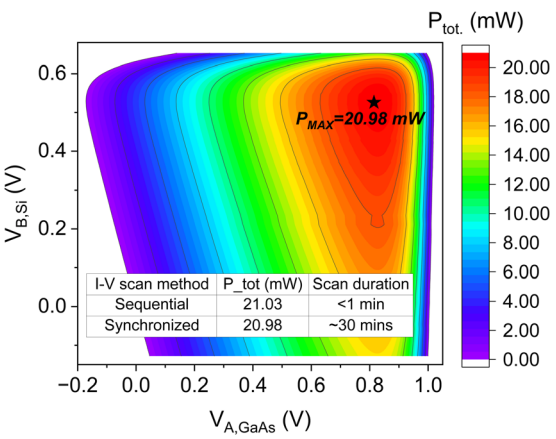

Fig. 4 Power contour plot of a GaAs/Si 4-T tandem solar cell measured as a function of $V_{A,GaAs}$ and $V_{B,Si}$ with synchronized *I–V* scans on both subcells. The insert table lists the total power and scan duration measured with both synchronized and sequential *I–V* scans.

method, but will also capture the off-peak operating conditions of the 4-T tandem. Fig. 4 illustrates the power contour plot of a mechanically-stacked GaAs/Si 4-T cell as a function of $V_{A,GaAs}$ and $V_{B,Si}$. As shown in the insert table, the peak power of 20.98 mW from the contour plot agrees closely (*i.e.*, within less than 0.2%, well below the measurement error of ~1.0%) with the combined total power (21.03 mW) obtained from the sequential *I–V* scans (shown in Fig. S2 in the supplemental file), in which both subcells operate at their respective P_{MAX} conditions.

This confirms that the two measurement approaches are effectively equivalent for determining device performance. However, a key drawback of the synchronized scan is its significantly lower measurement throughput: the matrix of *I–V* arrays requires more than 30 minutes to complete in this case, compared to less than one minute for the sequential *I–V* scans.

3.3 Dynamic-response devices

While synchronized *I–V* scans are well-suited for characterizing the performance of conventional III–V and Si-based 3-T and 4-T tandem cells, they present significant challenges for emerging multi-terminal devices based on perovskites. These challenges arise from their slow response to change in the operating condition (such as voltage bias), which causes the current–voltage scan to depend on scan rate and scan direction.[16,28,29] Additionally, perovskite performance is affected by pre-conditioning, which is not yet fully understood and varies across different material formulations and device history. For example, Fig. 5 shows two power contour plots of a perovskite(PVSK)/Si 3-T tandem cell as a function of $V_{TZ,PVSK}$ and $V_{RZ,Si}$, measured under both forward (from I_{SC} to V_{OC}) and reverse (from V_{OC} to I_{SC}) scans on both subcells, using a voltage step of ~5–10 mV and a delay between steps of ~100 ms. This cell is a pseudo 3-T device assembled with an encapsulated perovskite cell and a 780 nm long-pass filtered Si cell at NREL, which shares a common extra "Z" lead by connecting the perovskite's negative lead to the Si's positive lead. The extracted P_{MAX} differs by more than 5% between the two scan directions, demonstrating that conventional *I–V* scans are not reliable for evaluating their performance, similar to what has been observed in 2-T single-junction or tandem perovskite cells.[16,17,28–30]

To accurately capture the dynamic behaviour of such slow-responding multi-terminal tandems, time must be introduced as an additional variable alongside the two load voltages, as expressed in eqn (6). In this case, stability of the measured quantity (current, power) over time is evaluated with the goal of reaching a steady-state (or stabilized) value. For meaningful performance comparisons, steady-state measurement methods already widely used for 2-T solar cells such as asymptotic *I–V* scan[16] and maximum power point tracking (MPPT),[29] can be adapted for 3-T and 4-T perovskite-based tandem configurations as discussed in the following.

For 3-T perovskite-based tandem cells, we propose two steady-state performance measurement methods that directly address their dynamic current response:

(1) Two-dimensional MPPT. This method continuously tracks both subcells' P_{MAX} by applying a "perturb-and-observe" algorithm to each subcell in a stepwise manner. This process is repeated until both subcells converge to stabilized P_{MAX} outputs (further details in section 3.3.1).

(2) Hybrid "MPPT + asymptotic P_{MAX} scan". In this approach, MPPT is only applied to one subcell while the other subcell is held at a fixed voltage bias near its V_{MAX}, with its current monitored until stabilization. This process is repeated across a range of voltage biases near the second subcell's V_{MAX}. Finally, the DUT's overall P_{MAX} is extracted by combining the stabilized P_{MAX} values of both subcells through polynomial fitting (further details in section 3.3.2).

We demonstrate both methods on an encapsulated perovskite/IBC Si 3-T tandem cell with an active area of approximately 4 cm^2. The cell was fabricated at CSEM following the protocol described in a previous publication.[11] In brief, the

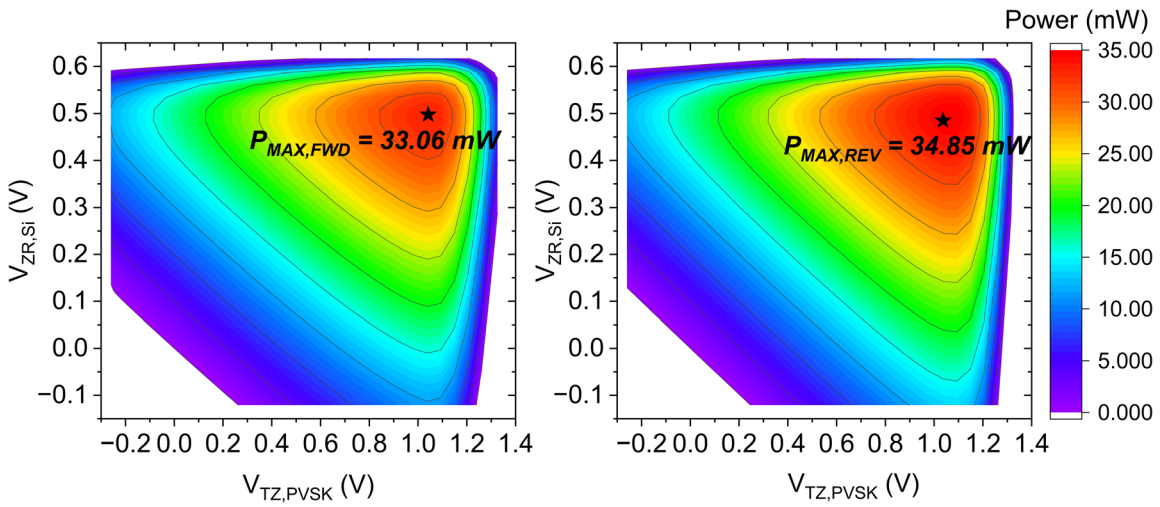

Fig. 5 3-D power plots of a perovskite/Si 3-T tandem cell as a function of $V_{TZ,PVSK}$ and $V_{ZR,Si}$ measured under (a) forward (from I_{SC} to V_{OC}) and (b) reverse (from V_{OC} to I_{SC}) scan directions on both subcells, respectively.

device consists of a p-i-n perovskite top cell grown directly on an n-type silicon heterojunction IBC bottom cell. Seven tandem cells, each measuring 4 cm^2, were produced on a 4-inch Si wafer and then separated by laser scribing. The busbars of the subcells were connected using ribbons, and the cells were encapsulated in a glass/glass package with lamination foils and an edge sealant.

3.3.1 Two-dimensional MPPT. In this approach, we employ a "perturb-and-observe" algorithm[29] using two SMUs: SMU A tracks $P_{MAX,PVSK}$ *via* terminals T and Z, while SMU B tracks $P_{MAX,Si}$ *via* terminals Z and R, as shown in Fig. 1a left. The procedure begins by applying two initial bias voltages (*i.e.*, $V_{A(TZ,PVSK)} = 0.9$ V and $V_{B(ZR.Si)} = 0.5$ V in Fig. 6a), chosen to be close to each subcell's V_{MAX}. Fig. 6a illustrates the corresponding voltage points ($V_{A(TZ,PVSK)}$ and $V_{B(ZR.Si)}$) during the MPPT tracking process, projected onto the power contour plot derived from the synchronized conventional *I–V* scans of the perovskite/IBC Si 3-T cell.

The algorithm first perturbs the top perovskite subcell's voltage bias $V_{A(TZ,PVSK)}$ by a predefined increment ΔV_A and records the corresponding change in output power, ΔP_A, while keeping the bottom Si subcell at its initial bias voltage. If $\Delta P_A > 0$, the perturbation continues in the same direction; if $\Delta P_A < 0$, the sign of ΔV_A is reversed. The same process is then applied to the bottom Si subcell to determine its next voltage bias $V_{B(ZR,Si)}$ while keeping the top perovskite subcell at its corresponding perturbed voltage bias. This iteration is repeated in a stepwise manner with this algorithm until both subcells converge to their stabilized P_{MAX} values (Fig. 6b), corresponding to the converged voltage perturbations shown in the insert of Fig. 6a.

To accommodate the slow response of the perovskite subcell, a 1 second delay is introduced between each voltage bias change, allowing the current to settle before the next voltage is applied.[29] Following the stabilization criterion used for 2-T perovskite devices,[29] we consider the power stabilized when it changes by <0.1%/min for at least 30 s after a minimum measurement time of 5 minutes. The device's total rated power is then obtained by averaging over the last 30 s (grey region in Fig. 6b).

3.3.2 Hybrid MPPT + asymptotic P_{MAX} scan. In this approach, the tandem power is determined by combining MPPT with asymptotic scans. First, the P_{MAX} of the subcell with weaker or little dynamic response (the Si subcell in the case of a 3-T perovskite/IBC Si cell) is estimated from a conventional *I–V* scan while leaving the terminal of the other subcell at open-circuit. From this scan, a set of voltage biases, $V_{ZR,Si}$ ranging from 0.50 V to 0.64 V as shown on the corresponding labels in Fig. 7, is selected in the vicinity of the Si subcell's V_{MAX}.[16]

While each $V_{ZR,Si}$ is held constant by SMU A and its measured current is recorded, an MPPT tracking process is simultaneously executed on the perovskite subcell using SMU B, following the same "perturb-and-observe" algorithm described in section 3.3.1. Each iteration continues until both stabilized $P_{TZ,PVSK}$ and $P_{ZR,Si}$ are achieved. The process is then repeated at the next $V_{ZR,Si}$ bias point, stepping through all selected voltage across the Si subcell's V_{MAX} range.

Fig. 7a and b show the evolution of subcell powers as a function of time under this hybrid scan process: the blue data points in Fig. 7a represent $P_{TZ,PVSK}$ tracked by MPPT at different $V_{ZR,Si}$ biases, while the yellow–green–purple data points in Fig. 7b illustrate the asymptotic behaviour of $P_{ZR,Si}$ at the same $V_{ZR,Si}$ biases near its V_{MAX}. Note that the dynamic current variations in the perovskite subcell are reflected in the bottom Si as they are coupled. Fig. 7c provides a closer snapshot of both subcells' power stabilization at one of the biases, $V_{ZR,Si} = 0.546$ V.

At each $V_{ZR,Si}$ bias point, the stabilization criterion requires that the power of both subcells change by <0.1%/min for at least 30 s after a minimum measurement time of 1 minute (grey area in Fig. 7c). Fig. 7d compiles all averaged power points meeting

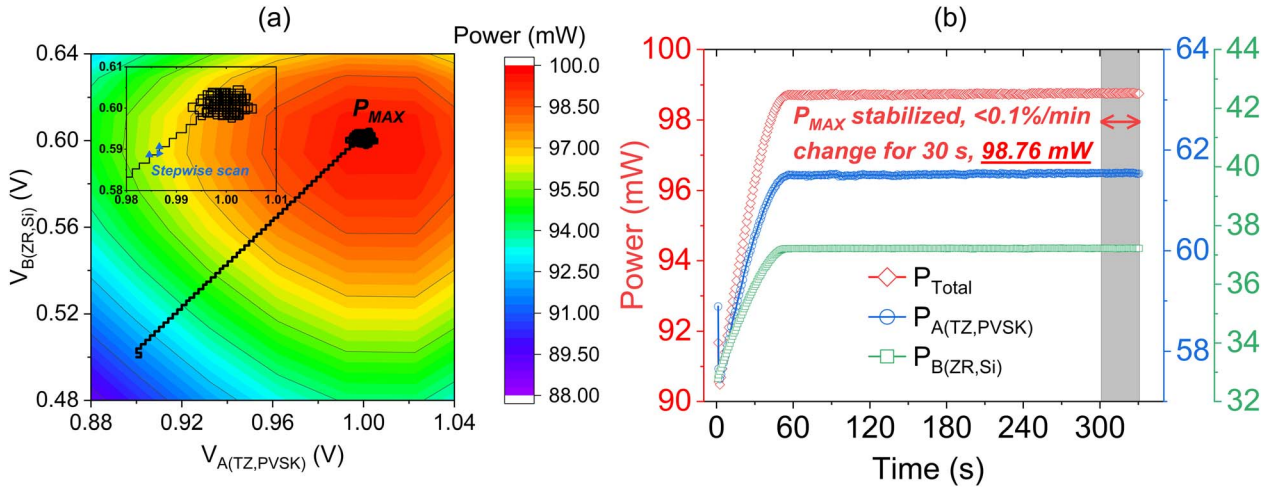

Fig. 6 2D MPPT characterization of 3-T perovskite/IBC silicon solar cell: (a) stepwise tracking voltages $V_{A(TZ,PVSK)}$ and $V_{B(ZR,Si)}$ obtained from the 2-D maximum-power-point tracking (MPPT) using the "perturb-and-observe" algorithm, projected onto the power contour plot derived from synchronized forward conventional *I–V* scans. The insert provides a closer view of the stepwise voltage perturbations approaching P_{MAX}. (b) Time evolution of the total power (P_{Total}), the subcell power ($P_{TZ,PVSK}$), and Si subcell power ($P_{ZR,Si}$) measured using the 2-D MPPT method.

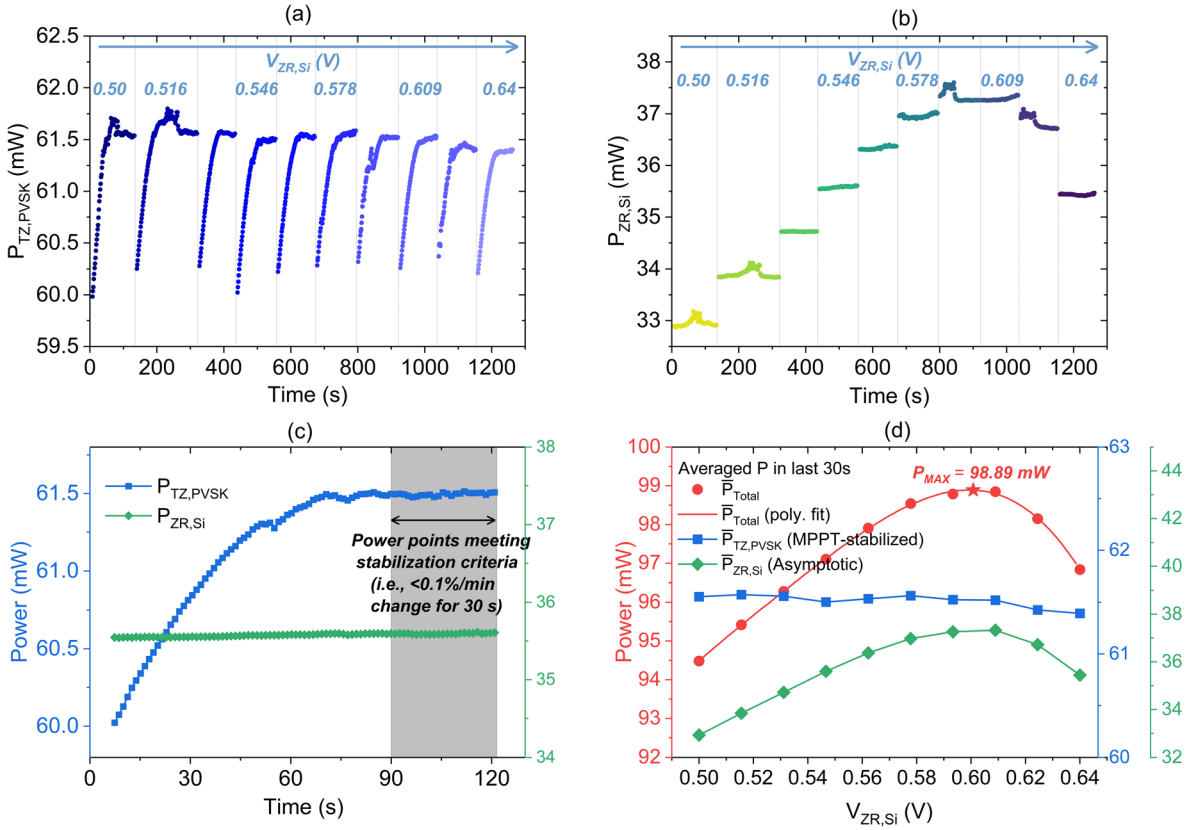

Fig. 7 Hybrid MPPT + asymptotic P_{MAX} scan characterization of 3-T perovskite/IBC silicon solar cell. (a) Power of the top perovskite subcell ($P_{TZ,PVSK}$) as a function of time, measured using MPPT at a set of fixed voltage biases $V_{ZR,Si}$ near the V_{MAX} of the Si subcell; (b) power of the corresponding bottom Si subcell ($P_{ZR,Si}$) as a function of time at such fixed voltage biases $V_{ZR,Si}$; (c) $P_{TZ,PVSK}$ and $P_{ZR,Si}$ as a function of time at $V_{ZR,Si}$ = 0.546 V; (d) averaged powers. $P_{TZ,PVSK}$ (MPPT-stabilized), $P_{ZR,Si}$, and P_{Total}, over the last 30 seconds, meeting stabilization criteria, as a function of $V_{ZR,SI}$, along with the polynomial fit of P_{Total} *vs.* $V_{ZR,Si}$, yielding P_{MAX} = 98.89 mW.

this criterion for both subcells, along with corresponding total power as a function of $V_{ZR,Si}$. Finally, a polynomial fit is applied to this dataset to determine the overall P_{MAX} of the 3-T tandem cell.

3.3.3 Results and implications. As shown in Fig. 6b and 7d, the total powers of the 3T perovskite/IBC Si tandem extracted *via* the two methods are 98.76 mW (2-D MPPT) and 98.89 mW (hybrid "MPPT + asymptotic P_{MAX} scan"), differing by <0.15%. This difference is well below our measurement uncertainty (~1%), confirming that both steady-state methods are equivalent for determining the performance of slow-responding 3-T tandems.

In terms of measurement throughput, 2-D MPPT (~6 min) is faster than the hybrid approach (~20 min), since it actively tracks both subcells' P_{MAX} in parallel. Both methods, however, are more efficient than synchronized conventional *I–V* scans, which require sweeping the entire voltage ranges of both subcells (*e.g.*, in our lab, the voltage range for each subcell is −0.05 × V_{OC} to 1.03 × V_{OC} depending on their V_{OC} values). For example, a conventional *I–V* scan typically involves ~200 points per subcell, each with a 100 ms delay. A synchronized 2-D *I–V* scan would thus require 200 × 200 × 0.1 s = 4000 s, *i.e.*, more than 1 hour.

More importantly, synchronized *I–V* scans cannot accurately capture the dynamic behaviour of slow-responding subcells, leading to potential measurement inaccuracies in the extracted performance metrics. By contrast, both steady-state methods overcome this limitation by allowing each subcell to reach equilibrium before recording power data, providing a more accurate representation of true operating performance. For example, the stabilized P_{MAX} of the perovskite/Si 3T device in Fig. 5 obtained from the hybrid method is 34.94 mW–higher than both the synchronized forward (33.06 mW) and reverse (34.85 mW) fast *I–V* sweeps. Conversely, for the perovskite/Si 3T cell in Fig. 6, the stabilized P_{MAX} (98.76 mW) is lower than its synchronized forward (99.61 mW) and reverse (99.29 mW) fast *I–V* sweeps, further illustrating the strong dependence of fast results on scan direction and measurement conditions.

Taken together, these results demonstrate that the two steady-state performance measurement methods not only enable reliable measurement of slow-responding tandems but can also be generalized to conventional 3-T tandems. If these approaches are available in a testing lab, they can offer both improved measurement reliability and substantially higher throughput.

For 4-T tandems containing a slow-responding subcell (*e.g.*, perovskite), the process is simpler than for 3-T devices, as the subcells can be measured sequentially (see section 3.2). The only adjustment required is to apply a steady-state method (MPPT or asymptotic P_{MAX} scan) to the slow-responding subcell.

4. Summary

Fig. 8 outlines a generalized framework for reliable performance evaluation of 3-T and 4-T tandem solar cells. The process begins with EQE measurements of the subcells, which are used to adjust the spectral irradiance of the simulator to ensure current matching to the reference spectrum and accurate photocurrent generation.

For 3-T tandems, synchronized *I–V* scans can be employed when both subcells exhibit fast response. If a slow-responding subcell is present (*e.g.*, perovskite), steady-state methods are required. Two options are proposed: (i) two-dimensional MPPT, which continuously tracks the power maxima of both subcells, or (ii) a hybrid method combining MPPT on one subcell with an asymptotic stabilized P_{MAX} scan on the other. Both approaches yield equivalent results but differ in measurement time.

For 4-T tandems, two *I–V* measurement approaches are possible: synchronized scans with spectrum adjustment or sequential scans with individual irradiance adjustment for each subcell. When slow-responding subcells are involved, they must be measured using steady-state methods, while fast-response subcells can be characterized with conventional *I–V* scans. In cases where luminescent coupling exists between subcells, the non-tested subcell must be held at its P_{MAX} using a proper load resistor to ensure accurate determination of the combined output.

It is important to note that not all research laboratories have access to spectrum-tuning hardware or synchronized scan capabilities. These limitations can introduce non-trivial measurable errors. For example, if separate *I–V* scans are used

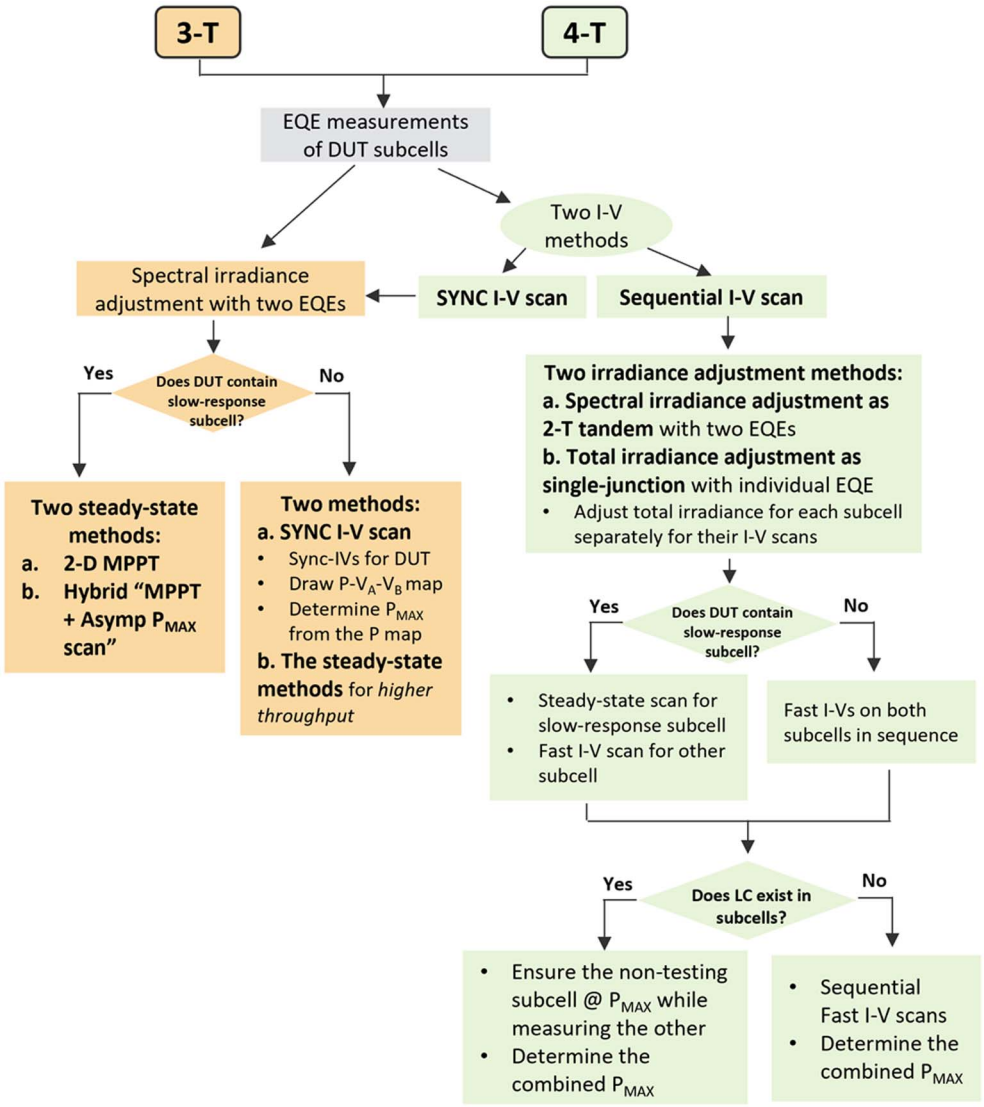

Fig. 8 Performance measurement framework of 3-T and 4-T tandem solar cells including devices containing slow-responding subcells.

instead of synchronized scans for the perovskite/IBC-Si 3-T device in Fig. 6, the extracted P_{MAX} can be overestimated by approximately 5% (103.59 mW from sequential forward scans *vs.* 98.76 mW from the 2-D MPPT method). As discussed in our previous work,[17] the absence of spectral tuning can similarly introduce significant measurement errors in tandem measurements. In situations where such capabilities are unavailable, results should be interpreted with caution:

(a) For record-seeking or accurate baseline measurements, spectrum tuning and synchronized steady-state performance methods are essential, and third-party evaluation by accredited testing labs is still highly recommended.

(b) For research and development stage measurements, simpler protocols–such as looser irradiance adjustment or non-synchronized *I–V* scans–may be used, but measurement limitations and potential sources of error should be clearly documented and reported.

Overall, this framework provides a clear strategy for adapting measurement methods to device architecture (3-T *vs.* 4-T), dynamic behaviour (fast *vs.* slow response), and optical interactions (presence of luminescent coupling), ensuring both accuracy and productivity in tandem solar cell characterization.

Author contributions

Conceptualization and investigation: T. S. Methodology: T. S., J. F. G., and N. K. Formal analysis: T. S. Writing – original draft: T. S., J. F. G., and N. K. Supervision, project administration, and funding acquisition: N. K. and T. S. Sample fabrication: J. F. G, K. V., L. L. S, F. S, L. C., J. G., B. P. S. and Q. J. Instrument development and maintenance: T. S., R. W., I. D., and J. B. Writing – review & editing: T. S., J. F. G., N. K., Q. J.

Conflicts of interest

There are no conflicts to declare.

Data availability

The data that support the findings of this article are not publicly available. The data are available from the authors upon reasonable request.

Supplementary information (SI): schematic diagrams of the three types of multi-terminal tandem cells investigated in this work, as well as representative light *I–V* curves of a GaAs/IBC Si 4-T device used in Fig. 4 measured using sequential fast *I–V* scans. The three tandem architectures studied are: (i) an epitaxially grown GaInP/GaAs 3-T cell, (ii) a mechanically stacked GaAs/IBC Si 4-T cell, and (iii) a perovskite/IBC Si 3-T cell. See DOI: https://doi.org/10.1039/d5el00195a.

Acknowledgements

The authors thank J. Gallon, C. Mack, R. Briggs, and A. Anderberg for results discussion. T. Song greatly acknowledges Robby Peibst and Michael Rienäcker at ISFH (Germany) for their generous permission to use the Si bottom cell data in the 4-T GaAs/Si testing. T. Song also thanks Fengjiu Yang at NREL for providing the encapsulated perovskite cell and Christian Wolf at EPFL for facilitating the collaboration with CSEM. CSEM would like to acknowledge P. Wyss, J. D. Decoppet, A. Theytaz, M. De Bastiani for help regarding device processing. This work was authored by the National Laboratory of the Rockies, operated by Alliance for Energy Innovation, LLC, for the U.S. Department of Energy (DOE) under Contract No. DE-AC36-08GO28308. Funding provided by U.S. Department of Energy Office of Critical Minerals and Energy Innovation Solar Energy Technologies Office (SETO) Agreement No. 52783. The views expressed in the article do not necessarily represent the views of the DOE or the U.S. Government. The U.S. Government retains and the publisher, by accepting the article for publication, acknowledges that the U.S. Government retains a nonexclusive, paid-up, irrevocable, worldwide license to publish or reproduce the published form of this work, or allow others to do so, for U.S. Government purposes.

References

1 Best Research-Cell Efficiency Chart, Photovoltaic Research, NREL, https://www.nrel.gov/pv/cell-efficiency, accessed August 20, 2025.
2 M. A. Green, E. D. Dunlop, M. Yoshita, N. Kopidakis, K. Bothe, G. Siefer, X. Hao and J. Y. Jiang, *Prog. Photovoltaics Res. Appl.*, 2025, **33**, 795–810.
3 F. Gota, M. Langenhorst, R. Schmager, J. Lehr and U. W. Paetzold, *Joule*, 2020, **4**, 2387–2403.
4 M. A. Steiner, M. W. Wanlass, J. J. Carapella, A. Duda, J. S. Ward, T. E. Moriarty and K. A. Emery, *Prog. Photovoltaics Res. Appl.*, 2009, **17**, 587–593.
5 I. J. Park, J. H. Park, S. G. Ji, M.-A. Park, J. H. Jang and J. Y. Kim, *Joule*, 2019, **3**, 807–818.
6 T. Tayagaki, K. Makita, T. Tachibana, H. Mizuno, R. Oshima, H. Takato and T. Sugaya, *Sol. Energy Mater. Sol. Cells*, 2021, **221**, 110901.
7 S. Essig, C. Allebé, T. Remo, J. F. Geisz, M. A. Steiner, K. Horowitz, L. Barraud, J. S. Ward, M. Schnabel, A. Descoeudres, D. L. Young, M. Woodhouse, M. Despeisse, C. Ballif and A. Tamboli, *Nat. Energy*, 2017, **2**, 17144.
8 M. Schnabel, H. Schulte-Huxel, M. Rienäcker, E. L. Warren, P. F. Ndione, B. Nemeth, T. R. Klein, M. F. A. M. van Hest, J. F. Geisz, R. Peibst, P. Stradins and A. C. Tamboli, *Sustainable Energy Fuels*, 2020, **4**, 549–558.
9 T. Nagashima, K. Okumura, K. Murata, and Y. Kimura, in *Conference Record of the Twenty-Eighth IEEE Photovoltaic Specialists Conference – 2000 (Cat. No.00CH37036)*, 2000, pp. 1193–1196.
10 K. T. VanSant, J. Simon, J. F. Geisz, E. L. Warren, K. L. Schulte, A. J. Ptak, M. S. Young, M. Rienäcker, H. Schulte-Huxel, R. Peibst and A. C. Tamboli, *ACS Appl. Energy Mater.*, 2019, **2**, 2375–2380.
11 M. Kikelj, L.-L. Senaud, J. Geissbühler, F. Sahli, D. Lachenal, D. Baetzner, B. Lipovšek, M. Topič, C. Ballif and Q. Jeangros, *Joule*, 2024, **8**, 852–871.

12 P. Tockhorn, P. Wagner, L. Kegelmann, J.-C. Stang, M. Mews, S. Albrecht and L. Korte, *ACS Appl. Energy Mater.*, 2020, **3**, 1381–1392.
13 R. C. Whitehead, K. T. VanSant, E. L. Warren, J. Buencuerpo, M. Rienäcker, R. Peibst, J. F. Geisz and A. C. Tamboli, *Appl. Phys. Lett.*, 2021, **118**, 183902.
14 T. Song, in *2020 47th IEEE Photovoltaic Specialists Conference (PVSC)*, IEEE, 2020, pp. 1941–1943.
15 J. F. Geisz, W. E. McMahon, J. Buencuerpo, M. S. Young, M. Rienäcker, A. C. Tamboli and E. L. Warren, *Cell Rep. Phys. Sci.*, 2021, **2**, 100677.
16 T. Song, D. J. Friedman and N. Kopidakis, *Adv. Energy Mater.*, 2021, **11**, 2100728.
17 T. Song, C. Mack, R. Williams, D. J. Friedman and N. Kopidakis, *Sol. RRL*, 2022, **6**, 2200800.
18 *G173 Standard Tables for Reference Solar Spectral Irradiances: Direct Normal and Hemispherical on 37° Tilted Surface*, https://store.astm.org/g0173-03r20.html, accessed August 20, 2025.
19 IEC 60904-3:2019|IEC, https://webstore.iec.ch/en/publication/61084, accessed August 20, 2025.
20 T. Song, C. Mack, J. Brewer, J. F. Geisz, R. Williams, D. J. Friedman and N. Kopidakis, *PRX Energy*, 2025, **4**, 033005.
21 T. Moriarty, J. Jablonski and K. Emery, in *2012 38th IEEE Photovoltaic Specialists Conference*, IEEE, 2012, pp. 001291–001295.
22 D. Chojniak, M. Schachtner, S. K. Reichmuth, A. J. Bett, M. Rauer, J. Hohl-Ebinger, A. Schmid, G. Siefer and S. W. Glunz, *Prog. Photovoltaics Res. Appl.*, 2024, **32**, 372–389.
23 M. Meusel, R. Adelhelm, F. Dimroth, A. W. Bett and W. Warta, *Prog. Photovoltaics Res. Appl.*, 2002, **10**, 243–255.
24 IEC 60904-1-1:2017|IEC, https://webstore.iec.ch/en/publication/29335, accessed August 20, 2025.
25 E2236 Standard Test Methods for Measurement of Electrical Performance and Spectral Response of Nonconcentrator Multijunction Photovoltaic Cells and Modules, https://store.astm.org/e2236-10r19.html, accessed August 20, 2025.
26 C. R. Osterwald, *Sol. Cell.*, 1986, **18**, 269–279.
27 E. L. Warren, W. E. McMahon, M. Rienacker, K. T. VanSant, R. C. Whitehead, R. Peibst and A. C. Tamboli, *ACS Energy Lett.*, 2020, **5**, 1233–1242.
28 T. Song, D. J. Friedman and N. Kopidakis, *Sol. RRL*, 2022, **6**, 2100867.
29 T. Song, L. Ottoson, J. Gallon, D. J. Friedman and N. Kopidakis, in *2021 IEEE 48th Photovoltaic Specialists Conference (PVSC)*, IEEE, 2021, pp. 0367–0371.
30 T. Song, T. Moriarty and D. Levi, in *2019 IEEE 46th Photovoltaic Specialists Conference (PVSC)*, IEEE, 2019, vol. 2, pp. 1–5.